

A Novel Coilless Scanning Mirror Using Eddy Current Lorentz Force and Magnetostatic Force

Hsueh-An Yang, Tsung-Lin Tang, Sheng Ta Lee, and Weileun Fang, *Member, ASME*

Abstract—This paper reports on novel coilless microscanning mirrors driven by the magnetostatic force that resulted from a magnetic interaction as well as the Lorentz force that is induced by an eddy current. This eliminates complicated coil routing and insulation layer deposition and simplifies fabrication allowing easy integration with micromachining and complementary metal-oxide-semiconductor processes. Bulk micromachined one-axis and two-axis scanning mirrors are demonstrated, displaying 1-D and 2-D scanning patterns. Two-dimensional scanning patterns are easily tuned by varying the combination of driving frequencies. The results show that the diamagnetic (*Cu*) mirror is mainly driven by the eddy-current-induced Lorentz force, whereas the ferromagnetic (*Ni*) mirror is mainly driven by the magnetostatic force. [2006-0082]

Index Terms—Eddy current, Lorentz force, magnetostatic force, scanning mirror.

I. INTRODUCTION

ELECTROMAGNETIC actuation, which is common in the macroworld, is a promising technique to drive microdevices. The noncontact electromagnetic actuator is able to deliver a large force and a large displacement. Applications of an electromagnetic force on microdevices have gradually been increasing over the past few years [1]. Presently, there are various approaches to generate the electromagnetic forces for microdevices [2]. For instance, the electromagnetic force reported in [3] results from the magnetic interaction of a permanent magnet and an external coil. In addition, an electroplated Permalloy has been employed in [4] to replace the permanent magnet. As a third example, the Lorentz force resulting from the interaction of an electric field and a magnetic field has been employed in [5]–[8] to drive microdevices. However, the current-induced magnetic force in [5]–[8] is limited to the

Manuscript received May 2, 2006; revised November 15, 2006. This work was supported in part by the National Science Council of Taiwan under Grant NSC-93-2218-E-007-012 and in part by the Ministry of Economic Affairs, Taiwan, under Contract 93-EC-17-A-07-S1-0011. Subject Editor D. DeVoe.

H.-A. Yang was with the Department of Power Mechanical Engineering, National Tsing Hua University, Hsinchu 30043, Taiwan, R.O.C. He is now with the Advanced Semiconductor Engineering Group, Kaohsiung 81166, Taiwan, R.O.C. (e-mail: d917706@alumni.nthu.edu.tw).

T.-L. Tang and S. T. Lee are with the Department of Power Mechanical Engineering, National Tsing Hua University, Hsinchu 30043, Taiwan, R.O.C. (e-mail: g943760@oz.nthu.edu.tw; g933778@oz.nthu.edu.tw).

W. Fang is with the Department of Power Mechanical Engineering, and with the Institute of Microelectromechanical Systems, National Tsing Hua University, Hsinchu 30043, Taiwan, R.O.C. (e-mail: fang@pme.nthu.edu.tw).

Color versions of one or more of the figures in this paper are available online at <http://ieeexplore.ieee.org>.

Digital Object Identifier 10.1109/JMEMS.2007.896708

design and fabrication of complicated coil routing and results in problematic joule heat generation.

An eddy current is defined as a closed-loop surface current induced by an alternating current (ac) magnetic flux [9]. Power loss due to an eddy current has been frequently discussed and applied in the macroworld. For instance, the induction heating caused by an eddy current has been extensively employed to heat electrically conductive bulk materials in applications such as melting, soldering, and hardening of metals [10]. The skin effect brought about by the eddy current is a design consideration for radio frequency components [11]. Currently, the eddy current has few applications in the microworld. A microelectromechanical system (MEMS)-based eddy current sensor has been reported in [12]. Localized induction heating due to an eddy current has been employed in [13] for a wafer-level MEMS package.

The two-axis micromachined scanning mirror is a key enabling component for optical applications such as the compact display system [14]. In general, the scanning mirror employs microactuators to manipulate incident light in two orthogonal directions. Thus, the design considerations include large scanning angle, high frequency response, and low driving voltages. Scanners driven by an electrostatic force have been extensively reported [15]–[17]. A scanner driven by piezo is available in [18]. Magnetic force is also introduced to drive the scanner in [19] and [20]. Electrical routing of the scanner is a critical issue not only for fabrication but also for packaging. The eddy current is exploited in this paper to generate the Lorentz force without conducting wire in an ac magnetic field. Meanwhile, the magnetostatic force will also be induced in the magnetic field to drive the scanner. The eddy current can be induced in metal, particularly ferromagnetic material (e.g., *Ni*) with higher permeability, by solenoid [21], eliminating the complicated coil routing and insulation layer deposition. In application, the coilless magnetic microactuators are demonstrated to drive *Ni* and *Cu* scanners.

II. CONCEPT

It is well known that a magnetic force F can be applied on a charged particle when it moves in a magnetic field B (in teslas). The force F is expressed as

$$F = qv \times B \quad (1)$$

where v is the velocity of the particle, and q is the magnitude (positive) of its charge. This equation is further employed to

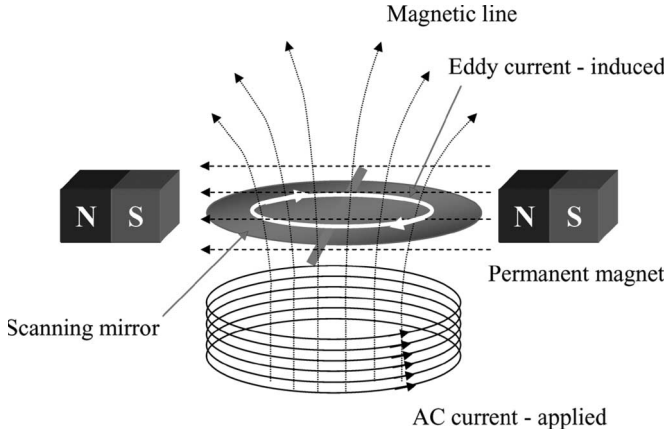


Fig. 1. Concept of coilless Lorentz force scanning mirror.

determine the magnetic force of a current-carrying wire that lies in a magnetic field, i.e.,

$$F = iL \times B \quad (2)$$

where i is the current carried by the wire, and L is the wire length. The concept of (2) has been extensively adopted to drive micromachined devices [22]. To this end, a more complicated microfabrication process is required to provide conducting wires.

A. Lorentz Force and Magnetostatic Force in AC Magnetic Field

The ac magnetic field has commonly been employed to generate an eddy current i_e in the workpiece for induction heating. This present paper adopts the same approach to generate the induced eddy current as well as the moving charged particles inside a conductor using an ac magnetic field. According to (1), these moving charged particles will introduce a magnetic force to the conductor when it is placed inside a magnetic field. Thus, the conducting wires and the additional complicated fabrication processes are no longer required. This paper further employs this magnetic force to drive a scanning mirror.

The design of the coilless Lorentz force scanning mirror is schematically illustrated in Fig. 1. The micromachined torsional mirror consists of torsional springs and a mirror plate with no coils. The torsional mirror is placed on top of a solenoid. In addition, the torsional mirror is also placed between two permanent magnets. A time-varying magnetic field is produced when an ac i with driving frequency ω is introduced into the solenoid, and the eddy current $i_e \sin \omega t$ is induced in the whole mirror plate. The magnitude of an eddy current i_e at a given radius r can be expressed as

$$i_e = \frac{\mu_0 \mu_r h r^2}{\rho} \omega n i \quad (3)$$

where h , μ_r , and ρ are the thickness, relative permeability, and resistivity of the mirror, respectively. The permeability constant

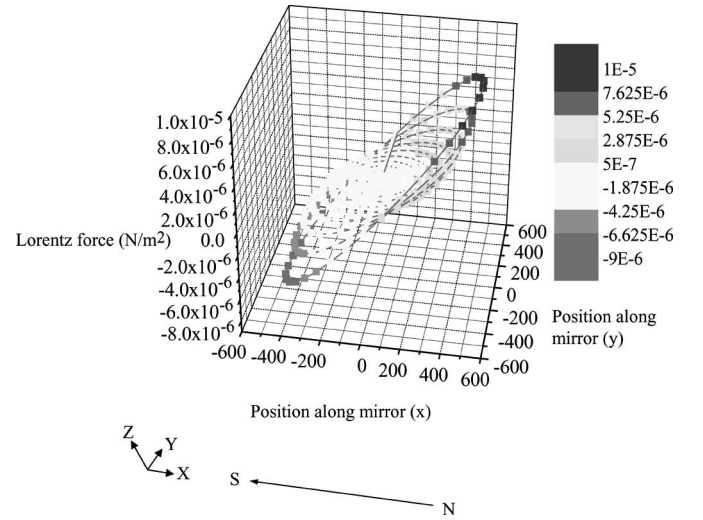


Fig. 2. Distribution of eddy current and Lorentz force.

μ_0 is $4\pi \times 10^{-7}$ (in henries per meter), and n is the number of turns per unit length. According to the magnetic field B_p that is introduced from permanent magnets, a time-varying Lorentz force $F_L \sin \omega t$ is developed on the mirror. The magnitude of force F_L on a particular point (r, θ) of the mirror can be expressed as

$$F_L = \frac{\mu_0 \mu_r h r^3}{\rho} \omega n i B_p \sin \theta \quad (4)$$

where θ is the angle between this point and the magnetic field B_p . The distribution of the Lorentz force is predicted in Fig. 2. The horizontal axes (x axis and y axis) indicate the position on the plate, whereas the vertical axis shows the magnitude of the Lorentz force F_L . Hence, the coil is no longer required for the present scanning mirror. The eddy current and the Lorentz force reach their maximum at the plate edge and their minimum at the plate center. Moreover, the magnetic flux and the intensity of the electromagnetic field vary with the area of the mirror plate [23]. It is easy to increase the intensity of the eddy current and the Lorentz force by increasing the planar dimensions of the mirror. In addition, a magnetostatic force $F_M \sin \omega t$ can also be applied on the scanner made of ferromagnetic material under the ac magnetic field, and

$$F_M = M A H_{\text{ext}} \quad (5)$$

where M , A , and H_{ext} are the magnetization, pole face area, and external magnetic field, respectively [24]. The magnetization M of a soft-magnetic material can be expressed as

$$M = \min \left(\frac{\mu_0 H_{\text{ext}} \cos(\gamma - \phi_m - \theta_0)}{\sqrt{N_a^2 \cos^2 \phi_m + N_c^2 \cos^2 \phi_m}}, M_s \right) \quad (6)$$

where γ is the angle between the original position and the magnetic field, ϕ_m is the angle between the magnetization direction and the easy axis, θ_0 is the maximum angular displacement of

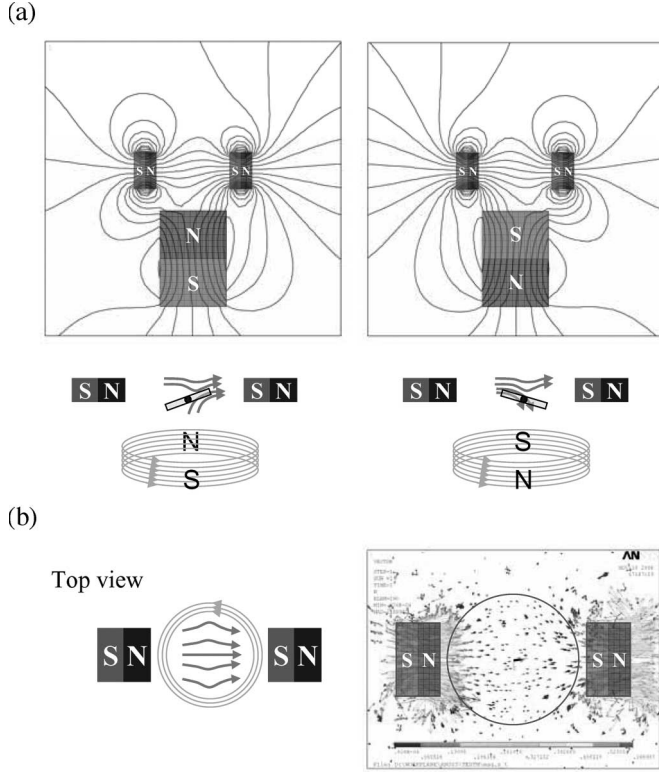


Fig. 3. Predicted magnetic field distribution. (a) Side view. (b) Top view.

the mirror, N_a and N_c are the shape anisotropy coefficients, and M_s is the saturation magnetization [25]. Since the magnetic field induced from the solenoid interacts with the field B_p , the distribution of a magnetic field will be significantly influenced by B_p . The simulation results in Fig. 3 predict the magnetic field distribution outside the solenoid with B_p . As indicated in Fig. 3(a), the mirror will be driven by the out-of-plane component of a magnetic field. The top view in Fig. 3(b) shows that the direction of the net magnetic field is mainly toward the direction of B_p .

B. Scanning Pattern of the One-Axis Coilless Scanner

The results in Fig. 2 indicate that the eddy-current-induced Lorentz force will generate an equivalent force couple on a symmetrical structure. Thus, the net force applied on the structure is zero, and a time-varying moment $M_L \sin \omega t$ is introduced by the Lorentz force. The direction of moment $M_L \sin \omega t$ is orthogonal to the direction of a magnetic field B_p . As shown in Fig. 4, the magnitude of moment M_L applied on the mirror with a radius r_m has the following form:

$$M_L = \frac{\pi \mu_0 \mu_r h r_m^4}{4\rho} \omega n i B_p. \quad (7)$$

In addition to the moment induced by the Lorentz force, a moment $M_M \sin \omega t$ that is due to a magnetostatic force F_M can also be applied on the scanner made of ferromagnetic material. According to the magnetic field distribution in Fig. 3,

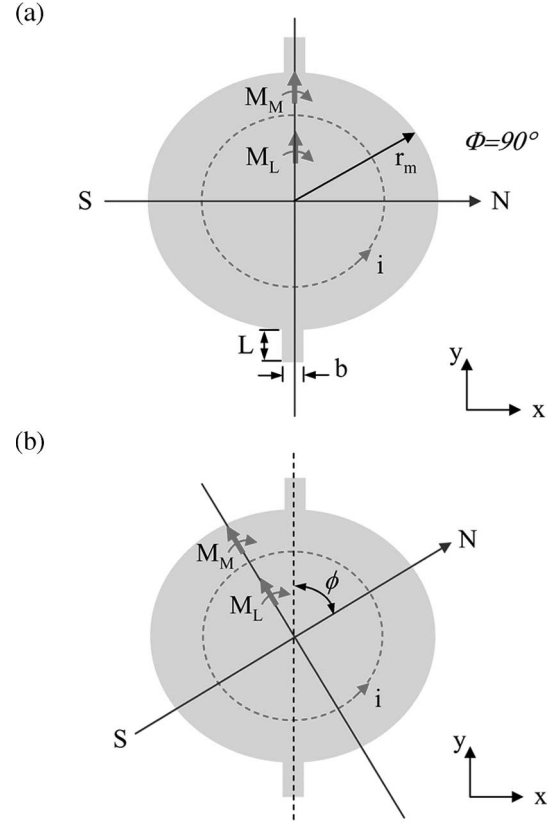


Fig. 4. Direction of induced moment for one-axis scanner when the magnetic field B_p has an intersection angle of ϕ with the springs. (a) $\phi = 90^\circ$. (b) $0^\circ < \phi < 90^\circ$.

the moment M_M is also orthogonal to the direction of B_p . Thus, the moment M_M , which is in the same direction with M_L , can be expressed as

$$M_M = \pi r_m^2 h n i M \sin(\gamma - \phi_{mm} - \theta_{m0}) \quad (8)$$

where ϕ_{mm} is the angle between the magnetization direction and the easy axis of the mirror, and θ_{m0} is the maximum angular displacement of the mirror. As shown in Fig. 4(a), the direction of B_p is aligned orthogonally to the springs. Thus, the net moment $(M_L + M_M) \sin \omega t$ will only introduce a twisting moment on the springs, so that the mirror with radius r_m will only scan the y axis. If the direction of B_p has an intersection angle of ϕ with the springs, as shown in Fig. 4(b), the moment $(M_L + M_M) \sin \omega t$ will not only introduce a twisting moment $(M_L + M_M) \sin \phi \sin \omega t$ but also a bending moment $(M_L + M_M) \cos \phi \sin \omega t$ on the springs. Hence, the mirror will be driven in both x and y axes. For a mirror with torsional stiffness K_t and bending stiffness K_b , its equations of motion associated with the first y -axis and x -axis scanning modes are, respectively, expressed as

$$I_y \ddot{\theta}_y + K_t \theta_y = (M_L + M_M) \sin \phi \sin \omega t \quad (9)$$

$$I_x \ddot{\theta}_x + K_b \theta_x = M_L + M_M \cos \phi \sin \omega t \quad (10)$$

where I_x and I_y represent mass moments of inertia of the mirror plate about the x and y axes, respectively. The stiffness

K_t and K_b of suspension with thickness h can be expressed as [26]

$$k_t = \frac{Gb h^3}{16L} \left[\frac{16}{3} - 3.36 \frac{h}{b} \left(1 - \frac{1}{12} \frac{h^4}{b^4} \right) \right] \quad (11)$$

$$k_b = \frac{2Ebh^3}{3L} \quad (12)$$

where b and L , as indicated in Fig. 4(a), represent the width and length of the suspension, respectively. In addition, the parameters G and E are the shear modulus and elastic modulus of the film, respectively. Thus, the mirror will experience a large scanning angle when it operates at the resonance frequencies of scanner $\omega_1 = \sqrt{(K_t/I_y)}$ or $\omega_2 = \sqrt{(K_b/I_x)}$. The angular displacements $\theta_x = \Theta_x \sin \omega t$ and $\theta_y = \Theta_y \sin \omega t$ have maximum mechanical scanning angles Θ_x and Θ_y , i.e.,

$$\Theta_x = \frac{(M_L + M_M) \cos \phi}{K_b \left(1 - \frac{\omega^2}{\omega_2^2} \right)} \quad (13)$$

$$\Theta_y = \frac{M_L + M \sin \phi}{K_t \left(1 - \frac{\omega^2}{\omega_1^2} \right)}. \quad (14)$$

In short, the scanning pattern of the present coilless scanner can be easily tuned by varying the magnetic fields, for instance, the intensity and frequency of the ac introduced into the solenoid, and the direction of the permanent magnets ϕ . The scanner will provide horizontal and vertical 1-D scanning patterns when $\phi = 0^\circ$ and 90° , respectively. The scanner will provide 2-D scanning patterns for the rest of angle ϕ . Considering a circular mirror with $I_x = I_y$ will lead to the amplitude ratio $\Theta_0 (= \Theta_x/\Theta_y)$ of

$$\Theta_0 = \frac{\cos \phi \omega_1^2 - \omega^2}{\sin \phi \omega_2^2 - \omega^2}. \quad (15)$$

Thus, the 2-D scanning pattern of a particular one-axis scanner can still be easily realized and tuned by varying the direction of the permanent magnets ϕ .

C. Scanning Pattern of the Two-Axis Coilless Scanner

The concept can be further applied to drive the two-axis gimbal scanner illustrated in Fig. 5. This gimbal scanner (with radius r_m) has a mirror plate connected to a hollow circular frame (with inner radius r_{fi} and outer radius r_{fo}) by springs K_m . The hollow circular frame also connects to fix ends by springs K_f . The springs K_m are aligned orthogonally to springs K_f . As shown in Fig. 5(a), the direction of B_p is aligned along the direction of springs K_f (i.e., $\phi = 90^\circ$). Thus, the net moment $M_{mL} \sin \omega t$ resulting from the eddy current on the mirror plate will introduce a twisting moment on springs K_m . The magnitude of moment M_{mL} can be yielded from (7). In addition, the net moment $M_{fL} \sin \omega t$ resulting from the

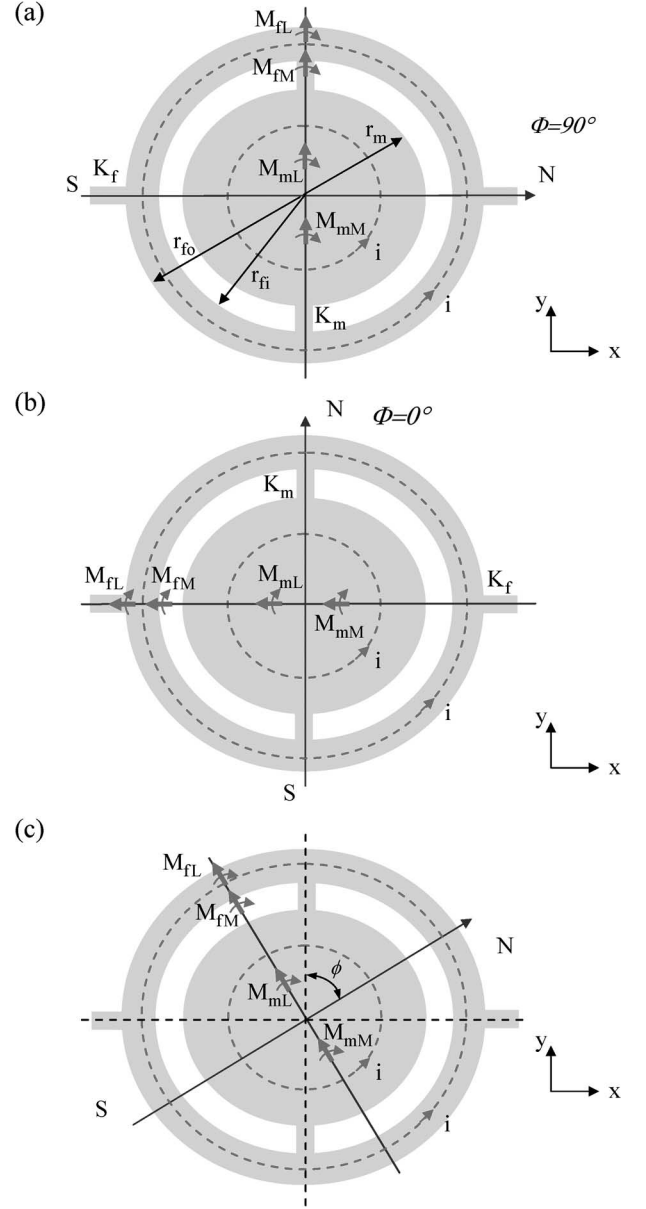


Fig. 5. Direction of induced moment for two-axis scanner when the magnetic field B_p has an intersection angle of ϕ with the springs. (a) $\phi = 90^\circ$. (b) $\phi = 0^\circ$. (c) $0^\circ < \phi < 90^\circ$.

eddy current on the frame will introduce a bending moment on springs K_f . The magnitude of moment M_{fL} is expressed as

$$M_{fL} = \frac{\pi \mu_0 \mu_r h \left(r_{fo}^4 - r_{fi}^4 \right)}{4\rho} \omega n i B_p. \quad (16)$$

Similarly, a moment M_{mM} from a magnetostatic force can also be applied on the mirror, and which can be yielded from (8). Moreover, a moment M_{fM} from a magnetostatic force applied on the frame can be expressed as

$$M_{fM} = \pi \left(r_{fo}^2 - r_{fi}^2 \right) h n i M \sin(\gamma - \phi_{fm} - \theta_{f0}) \quad (17)$$

where ϕ_{fm} is the angle between the magnetization direction and the easy axis of the frame, and θ_{f0} is the maximum angular displacement of the frame. After combining the moments

generated from the Lorentz force and the magnetostatic force, the total moments are yielded as

$$M_m = M_{mL} + M_{mM} \quad (18)$$

$$M_f = M_{fL} + M_{fM}. \quad (19)$$

Considering the mirror and the frame as a rigid body, the equations of motion associated with the y -axis scanning modes for mirror θ_{my} and frame θ_{fy} are expressed as

$$\begin{cases} I_{my}\ddot{\theta}_{my} + K_{mt}(\theta_{my} - \theta_{fy}) = M_m \sin \omega t \\ I_{fy}\ddot{\theta}_{fy} + K_{fb}\theta_{fy} + K_{mt}(\theta_{fy} - \theta_{my}) = M_f \sin \omega t \end{cases} \quad (20)$$

where I_{my} and I_{fy} are mass moment of inertia about the y axis for mirror and frame, respectively, K_{mt} is the net torsional stiffness for springs K_m , and K_{fb} is the net bending stiffness for springs K_f . The angular displacements of the mirror θ_{my} and frame θ_{fy} obtained from (20) are given in (21) and (22), as shown at the bottom of the page. When the direction of B_p is aligned along the direction of springs K_m (i.e., $\phi = 0^\circ$), as indicated in Fig. 5(b), the equations of motion associated with the y -axis scanning modes for mirror θ_{mx} and frame θ_{fx} are expressed as

$$\begin{cases} I_{mx}\ddot{\theta}_{mx} + K_{mb}(\theta_{mx} + \frac{1}{2}\theta_{fx}) = M_m \sin \omega t \\ I_{fx}\ddot{\theta}_{fx} + K_{ft}\theta_{fx} + K_{mb}(\theta_{fx} + \frac{1}{2}\theta_{mx}) = M_f \sin \omega t \end{cases} \quad (23)$$

where I_{mx} and I_{fx} are mass moments of inertia about the x -axis for the mirror and frame, respectively, K_{mb} is the net bending stiffness for springs K_m , and K_{ft} is the net torsional stiffness for springs K_f . Similarly, the angular displacement θ_{mx} of the mirror can be obtained in (24) and (25), as shown at the bottom of the page. If the direction of B_p has an angle of $0^\circ < \phi < 90^\circ$, as shown in Fig. 5(c), the net moments in (20) become $M_m \sin \phi \sin \omega t$ and $M_f \sin \phi \sin \omega t$, and the net moments in (23) become $M_m \cos \phi \sin \omega t$ and $M_f \cos \phi \sin \omega t$.

In summary, the two-axis scanner has angular displacements of $\theta_x = \Theta_x \sin \omega t$ and $\theta_y = \Theta_y \sin \omega t$ with maximum mechanical scanning angles Θ_x and Θ_y , i.e.,

$$\Theta_x = (\theta_{my})_{\phi=90^\circ} \sin \phi \quad (26)$$

$$\Theta_y = (\theta_{mx})_{\phi=0^\circ} \cos \phi. \quad (27)$$

The scanner will provide horizontal and vertical 1-D scanning patterns when $\phi = 0^\circ$ and 90° , respectively. The scanner will provide 2-D scanning patterns for the rest of angle ϕ . Thus, the scanning patterns of the coilless two-axis scanner are realized and tuned by varying the intensity and frequency of the magnetic field, and the direction of the permanent magnets ϕ .

III. EXPERIMENT AND RESULTS

The process steps shown in Fig. 6 have been established in this paper to demonstrate the feasibility of the coilless scanning mirror. As shown in Fig. 6(a), the *Ti* adhesion layer and the *Cu* seed layer were deposited onto a silicon wafer. Fig. 6(b) shows that the *Cu* layer was patterned to define the window for the following bulk silicon etching. As shown in Fig. 6(c) and (d), a thick *AZ4620* photoresist acted as a mold after photolithography, and then a $20\text{-}\mu\text{m}$ -thick *Ni* was electroplated and molded. Fig. 6(e) shows the second molding process using the *AZ4620* photoresist and *Ni* film, so as to increase the thickness of some particular components such as the mirror plate. This key process enables structures with different thicknesses and stiffness. Table I lists the recipe of electroplating solutions for *Ni*. After stripping the photoresist, the *Ti* film, without protection from the *Cu* layer, was etched away by buffered oxide etchant and the silicon substrate underneath was exposed, as shown in Fig. 6(f). Finally, the *Ni* structure was released from the substrate after bulk silicon etching by tetramethyl ammonium hydroxide (*TMAH*), as depicted in Fig. 6(g). Following the similar process steps, the *Cu* scanning mirrors were also fabricated. However, the *Cu* structure was released from the

$$(\theta_{my})_{\phi=90^\circ} = \frac{-I_{fy}M_m\omega^2 + M_m(K_{fb} + K_{mt}) + M_fK_{mt}}{I_{my}I_{fy}\omega^4 - (K_{fb}I_{my} + K_{mt}I_{fy} + K_{mt}I_{my})\omega^2 - K_{mt}} \sin \omega t \quad (21)$$

$$(\theta_{fy})_{\phi=90^\circ} = \frac{-I_{my}M_f\omega^2 + M_mK_{mt} + M_fK_{mt}}{I_{my}I_{fy}\omega^4 - (K_{fb}I_{my} + K_{mt}I_{fy} + K_{mt}I_{my})\omega^2 - K_{mt}} \sin \omega t \quad (22)$$

$$(\theta_{mx})_{\phi=0^\circ} = \frac{-I_{fx}M_m\omega^2 + M_m(K_{ft} + K_{mb}) - \frac{1}{2}M_fK_{mb}}{I_{mx}I_{fx}\omega^4 - (K_{ft}I_{mx} + K_{mb}I_{fx} + K_{mb}I_{mx})\omega^2 - \frac{1}{4}K_{mb}^2} \sin \omega t \quad (24)$$

$$(\theta_{fx})_{\phi=0^\circ} = \frac{-I_{mx}M_f\omega^2 + M_fK_{mb} - \frac{1}{2}M_mK_{mb}}{I_{mx}I_{fx}\omega^4 - (K_{ft}I_{mx} + K_{mb}I_{fx} + K_{mb}I_{mx})\omega^2 - \frac{1}{4}K_{mb}^2} \sin \omega t \quad (25)$$

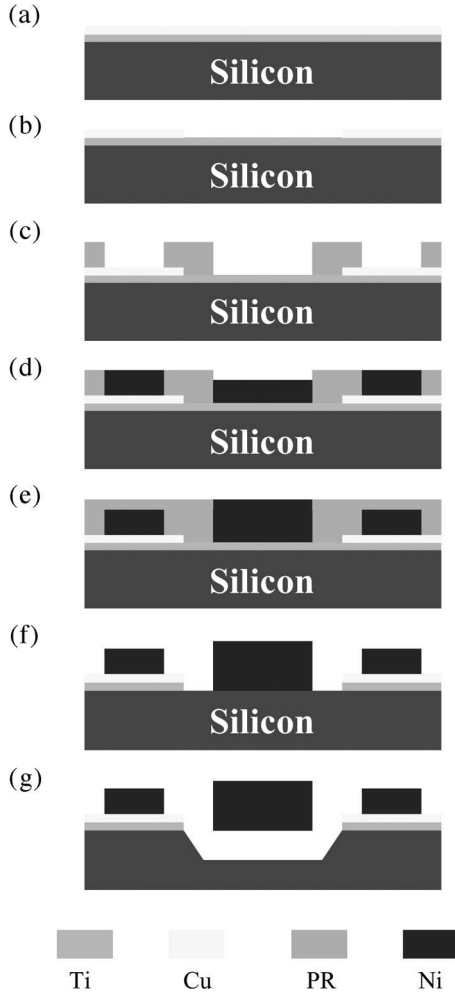


Fig. 6. Fabrication processes of coilless scanning mirror.

TABLE I
RECIPE OF ELECTROPLATING SOLUTIONS FOR NICKEL

Nickel Sulfamate $\text{Ni}(\text{NH}_2\text{SO}_4)_2 \cdot 4\text{H}_2\text{O}$	450~550 g/l
Nickel Chloride $\text{NiCl}_2 \cdot 6\text{H}_2\text{O}$	2~7 g/l
Boric Acid H_3BO_3	30~50 g/l
Stress Reducer	2~10 ml/l

substrate by means of deep reactive ion etching for backside etching and then dipped into *TMAH* for polishing.

Fig. 7 shows the scanning electron microscope (SEM) photos of typical fabrication results. The one-axis gimbal scanning mirror in Fig. 7(a) consists of a mirror plate and one pair of torsional springs. This SEM photo clearly demonstrates the coilless mirror plate design. The mirror connects to the substrate through the torsional springs. The K_t and K_b in (11) and (12) are determined, respectively, by the torsional and bending stiffnesses of the torsional spring. The rigid frame and mirror

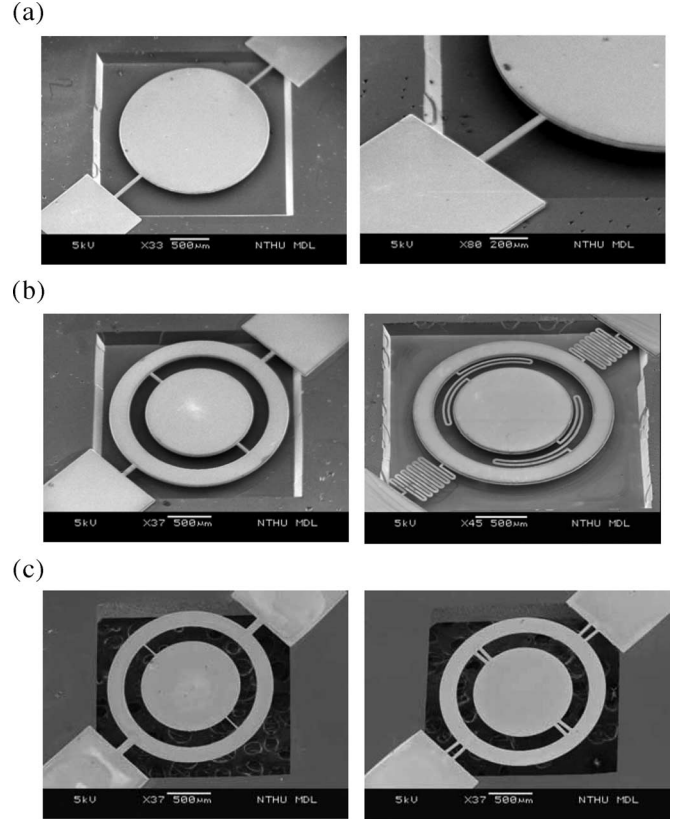


Fig. 7. SEM photos of typical fabrication results. (a) One-axis *Ni* scanner. (b) Two-axis *Ni* scanner. (c) Two-axis *Cu* scanner.

plate (2000 μm in diameter) were 18 μm in thickness, whereas the flexible spring was only 8 μm thick. The thickness difference of the mirror plate and springs can be easily observed in the zoomed-in photo in Fig. 7(a). According to the bulk silicon etching, the space under the scanner was 150 μm . The surface roughness of the electroplated *Ni* mirror measured by an atomic force microscope was about 10.2 nm. The thickness variation across the mirror plate measured by optical interferometer is less than 1%. The two-axis gimbal scanning mirrors in Fig. 7(b) consist of a mirror plate, a supporting frame, and two pairs of torsional springs. The shape as well as stiffness of the torsional springs can be easily tuned by the process. The mirror connects to the supporting frame through one pair of springs, and the supporting frame connects to the substrate through another pair of springs. The design of these two pairs of springs allows the mirror and the supporting frame to be flexible in the orthogonal directions. As a comparison, the photos in Fig. 7(c) show the suspended *Cu* mirrors.

Fig. 8 shows the experimental setup for the driving test of the mirror. In this paper, the strength of the permanent magnet was near 2870 G. The ac magnetic field provided by the solenoid was about 3.7 G when the carried current was 17 mA. The dynamic characteristics of the scanner are measured by varying with the driving frequency of the ac magnetic field. Moreover, the solenoid can be driven by various function generators, so that it can provide the ac magnetic field with multiple excitation frequencies. Thus, more than one resonant mode of scanner can be excited by the present driving mechanism. Fig. 9 shows

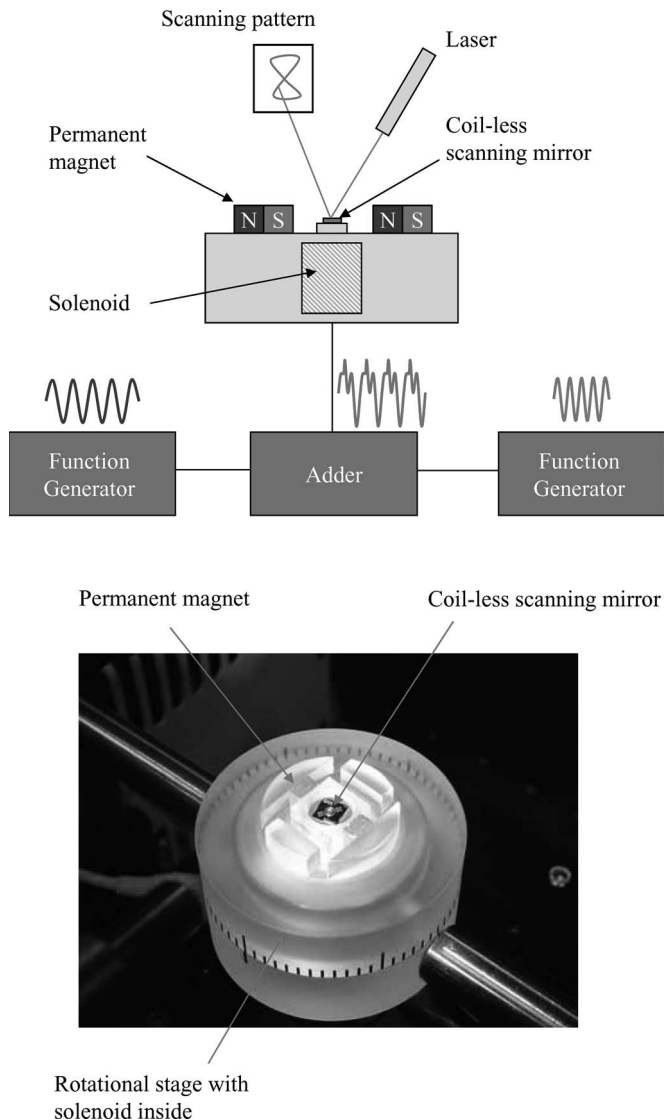


Fig. 8. Schematic illustration and photo of the experiment setup for mirror driving test.

the typical measured frequency responses of one-axis and two-axis *Ni* scanners. As shown in Fig. 9(a), the two orthogonal scanning resonant modes of the one-axis scanner are 838 Hz (torsional mode of spring) and 3912 Hz (bending mode of spring), respectively. As shown in Fig. 9(b), the two orthogonal scanning resonant modes were 2708 Hz (torsional mode of frame) and 4920 Hz (torsional mode of mirror), respectively. It demonstrates that the eddy-current-induced Lorentz force and the magnetostatic force were not only applied at the mirror plate but also at the supporting frame, as illustrated in Fig. 5. The typical optical scan angle was 20° at an input power of 9 mW. Thus, both of the one-axis and two-axis scanners can provide 2-D scanning patterns. The scanning angle of *Ni* mirror had dropped slightly after removing the permanent magnets (i.e., remove B_p and the induced Lorentz force). In other words, the *Ni* (ferromagnetic material) scanning mirror was mainly driven by the magnetostatic force. As a comparison, Fig. 10 shows the typical measured frequency responses of a two-axis *Cu* scanner. The scanning angle of the *Cu* (diamagnetic material) scanner

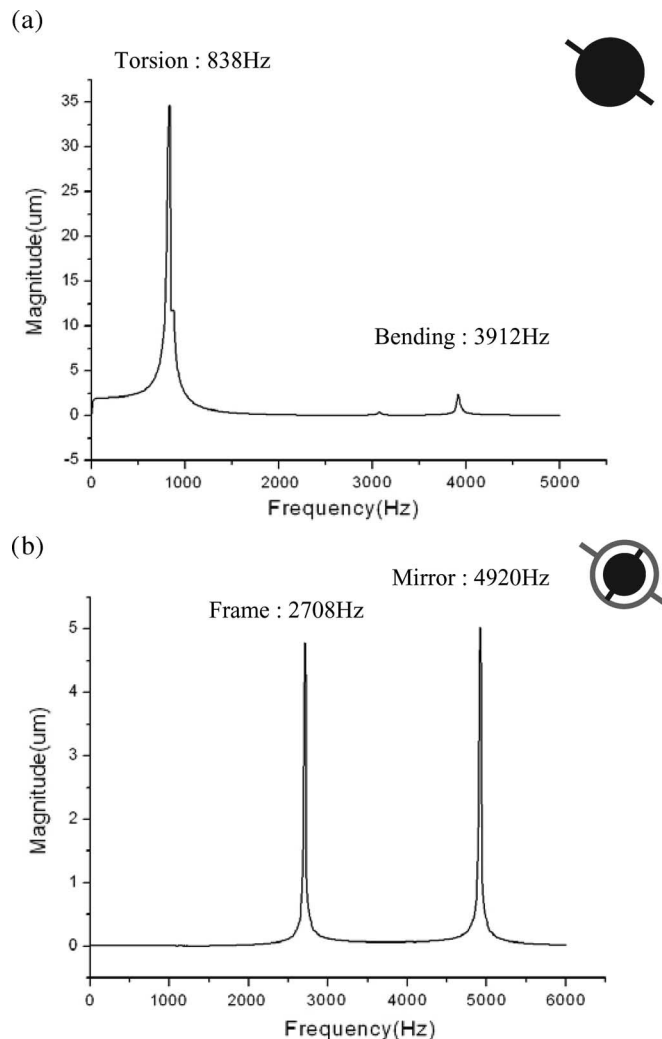


Fig. 9. Typical measured frequency responses for (a) one-axis scanner and (b) two-axis scanner.

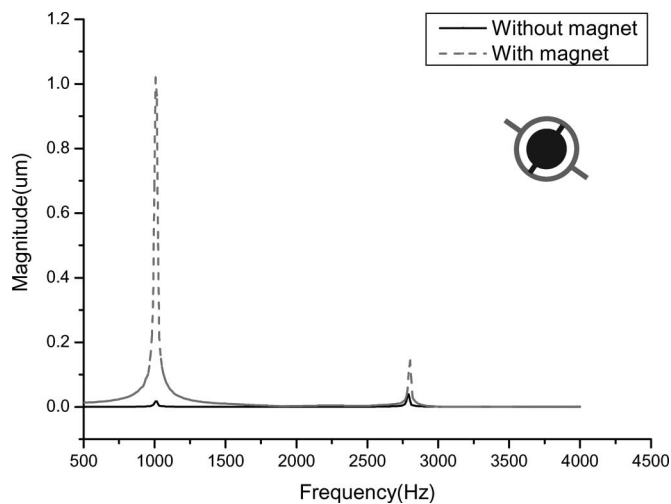


Fig. 10. Typical measured frequency responses for 2-D *Cu* scanner.

is much smaller than that of the *Ni* (ferromagnetic material) scanner. In addition, the response with a magnetic field B_p (dashed line) is much higher than that without B_p (solid line). It demonstrates that the *Cu* (diamagnetic material) scanning

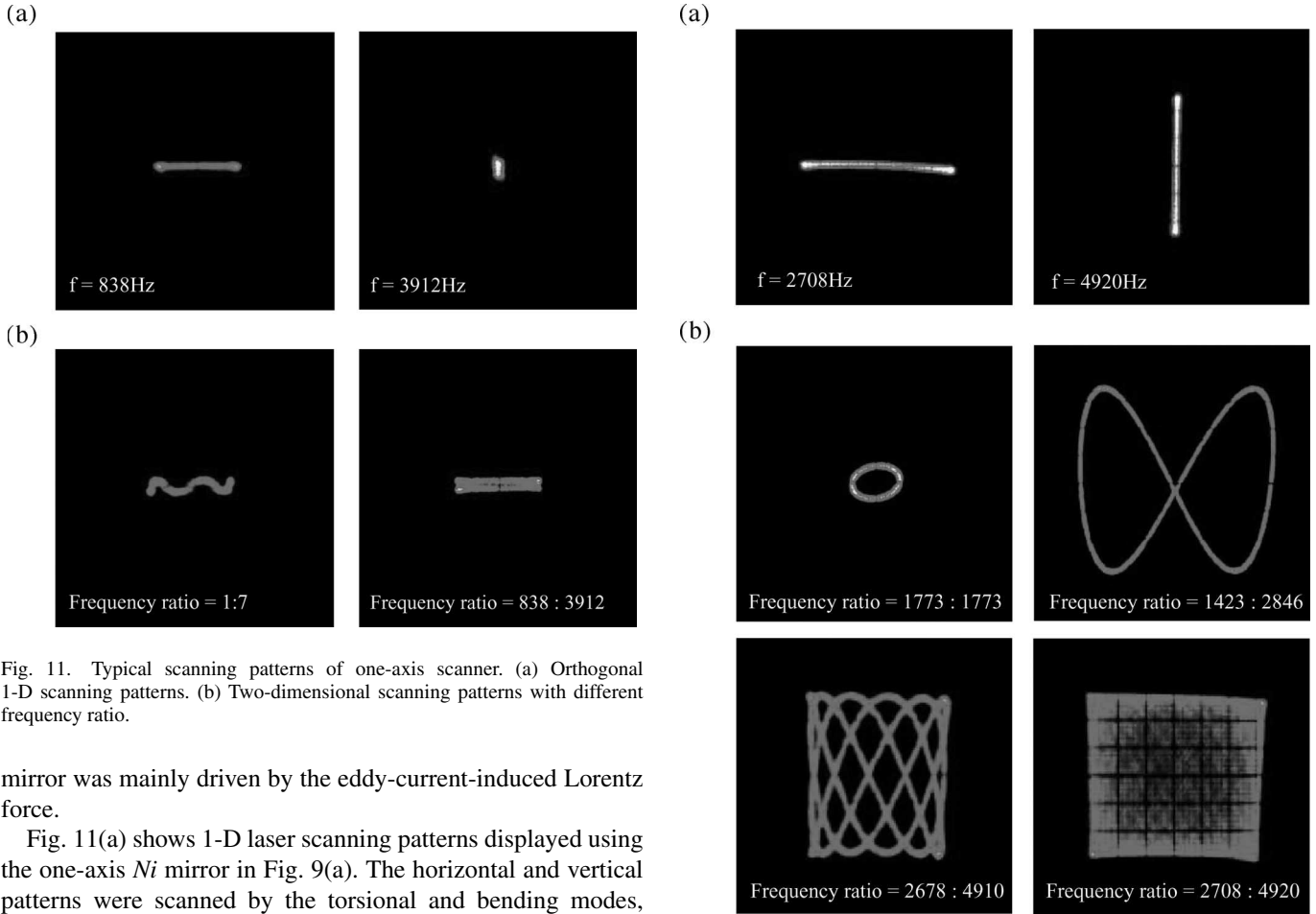


Fig. 11. Typical scanning patterns of one-axis scanner. (a) Orthogonal 1-D scanning patterns. (b) Two-dimensional scanning patterns with different frequency ratio.

mirror was mainly driven by the eddy-current-induced Lorentz force.

Fig. 11(a) shows 1-D laser scanning patterns displayed using the one-axis *Ni* mirror in Fig. 9(a). The horizontal and vertical patterns were scanned by the torsional and bending modes, respectively. According to (11) and (12), the stiffness K_b is approximately one order of magnitude larger than the stiffness K_t ; therefore, the scanning angle associated with the bending mode was smaller. Both of these two orthogonal scanning modes were excited simultaneously when the solenoid was driven by dual ac signals. Thus, the 2-D scanning patterns are achieved, as indicated in Fig. 11(b), and the frequency ratios were 1 : 7 and 838 : 3912, respectively. Fig. 12(a) shows 1-D laser scanning patterns when the two-axis *Ni* mirror in Fig. 9(b) was driven at its orthogonal scanning modes, respectively. The horizontal scanning pattern was displayed by the frame torsional mode (2708 Hz), whereas the vertical one was scanned by the mirror torsional mode (4920 Hz). This paper also employed dual frequencies to simultaneously drive the mirror and frame torsional modes. Thus, the 2-D scanning patterns are displayed, as shown in Fig. 12(b). The 2-D scanning patterns were easily tuned by varying the combination of these two driving frequencies. As indicated in Fig. 12(b), the frequency ratios were 1 : 1 (1773 : 1773 Hz), 1 : 2 (1423 : 2846 Hz), 2678 : 4910, and 2708 : 4920 (frame and mirror torsional modes), respectively.

This paper also demonstrates the tuning of scanning patterns by varying the direction of the permanent magnets ϕ , as presented in Section II. Fig. 13 shows the scanning patterns for 16 different directions of a magnetic field B_p . In short, the scanning pattern of the present coilless scanner can be tuned by varying not only the structure design and driving frequency but also the direction of permanent magnetic field B_p . The

Fig. 12. Typical scanning patterns of two-axis scanner. (a) Orthogonal 1-D scanning patterns. (b) Two-dimensional scanning patterns with different frequency ratio.

measurement results agree with the simulation results shown in Fig. 3(b) that the direction of the net magnetic field is toward the direction of B_p , so that both of the moments M_L and M_M are orthogonal with the direction of B_p . The joule heat is one design consideration for the Lorentz force actuator. Fig. 14 shows the temperature distribution on the scanning mirror measured by an infrared microscope. Since the operating frequency ranges from 900 to 4000 Hz, the mirror had not been heated by an eddy current.

IV. SUMMARY

This paper reports on novel coilless micro scanning mirrors driven by the magnetostatic force that resulted from a magnetic interaction as well as the Lorentz force that is induced by an eddy current. The one-axis and two-axis scanning mirrors have been successfully fabricated and tested. Typical testing results showed that the optical scan angle was 20° when the scanner was operated at an input power of 9 mW. The present scanner has the following advantages and characteristics. First, complex current routing and insulation layer deposition for the Lorentz force is not required. Second, it is easy to drive the scanner using the far-field magnetic force, which no longer gives limitations to the scanning angle. Third, the fabrication processes

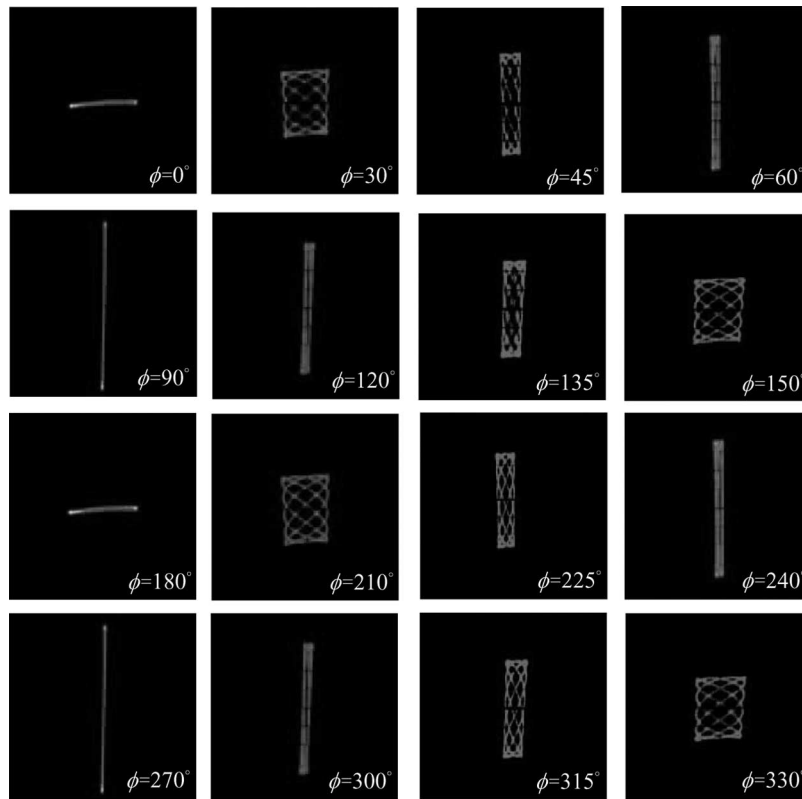


Fig. 13. Variation of the scanning patterns with the direction of the permanent magnets ϕ .

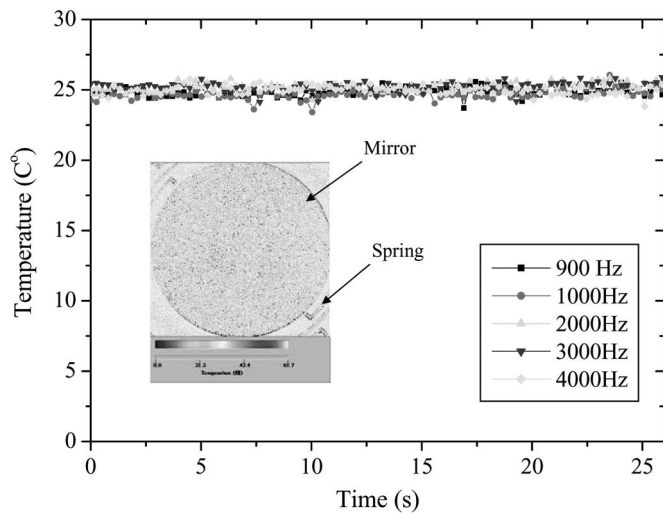


Fig. 14. Measured temperature distribution on scanning mirror during operation.

are simple and easy to integrate with micromachining and complementary metal–oxide–semiconductor processes. Fourth, the scanning pattern of the present coilless scanner can be tuned by varying the direction of the permanent magnetic field. Fifth, the induction heating by an eddy current on the scanner and the silicon substrate can be ignored for the operating frequency range. However, several issues are of concern while applying the coilless eddy current force. First, only an ac excitation is available for the scanner. Second, the fatigue of the metal film may lead to the resonant frequency drift of the scanner.

ACKNOWLEDGMENT

The authors would like to thank the NSC Central Regional MEMS Center, Taiwan, the Nano Facility Center of National Tsing Hua University, and the NSC National Nano Device Laboratory for providing fabrication facilities.

REFERENCES

- [1] J. W. Judy, R. S. Muller, and H. H. Zappe, "Magnetic microactuation of polysilicon flexure structures," *J. Microelectromech. Syst.*, vol. 4, no. 4, pp. 162–169, Dec. 1995.
- [2] T. M. Liakopoulos and C. H. Ahn, "3-D microfabricated toroidal planar inductors with different magnetic core schemes for MEMS and power electronic applications," *IEEE Trans. Magn.*, vol. 35, no. 5, pp. 3679–3681, Sep. 1999.
- [3] J. W. Judy and R. S. Muller, "Magnetically actuated, addressable microstructures," *J. Microelectromech. Syst.*, vol. 6, no. 3, pp. 249–256, Sep. 1997.
- [4] H. Guckel, "Progress in magnetic microactuators," *Microsyst. Technol.*, vol. 5, no. 2, pp. 59–61, Dec. 1998.
- [5] N. Asada, H. Matsuki, K. Minami, and M. Esashi, "Silicon micromachined two-dimensional galvano optical scanner," *IEEE Trans. Magn.*, vol. 30, no. 6, pp. 4647–4649, Nov. 1994.
- [6] H. Miyajima, N. Asaoka, M. Arima, Y. Minamoto, K. Murakami, K. Tokuda, and K. Matsumoto, "A durable, shock-resistant electromagnetic optical scanner with polyimide-based hinges," *J. Microelectromech. Syst.*, vol. 10, no. 3, pp. 418–424, Sep. 2001.
- [7] S. H. Ahn and Y. K. Kim, "Silicon scanning mirror of two DOF with compensation current routing," *J. Micromech. Microeng.*, vol. 14, no. 11, pp. 1455–1461, Nov. 2004.
- [8] J. J. Bernstein, W. P. Taylor, J. D. Brazzle, C. J. Corcoran, G. Kirkos, J. E. Odhner, A. Pareek, M. Waelti, and M. Zai, "Electromagnetically actuated mirror arrays for use in 3-D optical switching applications," *J. Microelectromech. Syst.*, vol. 13, no. 3, pp. 526–535, Jun. 2004.
- [9] B. D. Cullity, *Introduction to Magnetic Materials*. Reading, MA: Addison-Wesley, 1972.

- [10] D. John and S. Peter, *Induction Heating Handbook*. New York: McGraw-Hill, 1979.
- [11] B. D. Jensen, K. Saitou, J. L. Volakis, and K. Kurabayashi, "Fully integrated electrothermal multidomain modeling of RF MEMS switches," *IEEE Microw. Wireless Compon. Lett.*, vol. 13, no. 9, pp. 364–366, Sep. 2003.
- [12] D. J. Sadler and C. H. Ahn, "On-chip eddy current sensor for proximity sensing and crack detection," *Sens. Actuators A, Phys.*, vol. 91, no. 3, pp. 340–345, Jul. 2001.
- [13] H. A. Yang, M. C. Wu, and W. Fang, "Localized induction heating solder bonding for wafer level MEMS packaging," *J. Micromech. Microeng.*, vol. 15, no. 2, pp. 394–399, Feb. 2005.
- [14] H. Urey, F. DeWitt, P. Lopez, and J. Tauscher, "MEMS raster correction scanner for SXGA resolution retinal scanning display," *Proc. SPIE*, vol. 4985, pp. 106–114, 2003.
- [15] V. A. Aksyuk, F. Pardo, and D. J. Bishop, "Stress-induced curvature engineering in surface-micromachined devices," *Proc. SPIE*, vol. 3680, pp. 984–993, 1999.
- [16] D. S. Greywall, P. A. Busch, F. Pardo, D. W. Carr, G. Bogart, and H. T. Soh, "Crystalline silicon tilting mirrors for optical cross-connect switches," *J. Microelectromech. Syst.*, vol. 12, no. 5, pp. 708–712, Oct. 2003.
- [17] R. A. Conant, J. T. Nee, K. Lau, and R. S. Mueller, "A fat high-frequency scanning micromirror," in *Proc. Solid-State Sens. and Actuator Workshop*, Hilton Head, SC, 2000, pp. 6–9.
- [18] M. Ikeda, H. Goto, H. Totani, M. Sakata, and T. Yada, "Two-dimensional miniature optical-scanning sensor with silicon micro-machined scanning mirror," *Proc. SPIE*, vol. 3008, pp. 111–122, 1997.
- [19] D. W. Wine, M. P. Hesel, L. Jenkins, H. Urey, and T. D. Osborn, "Performance of a biaxial MEMS-based scanner for microdisplay applications," *Proc. SPIE*, vol. 4178, pp. 186–196, 2000.
- [20] H. Urey, A. D. Yalcinkaya, T. Montague, D. Brown, R. Sprague, O. Anac, C. Ataman, and I. Basdogan, "Two-axis MEMS scanners for display and imaging applications," in *Proc. IEEE-LEOS Opt. MEMS*, Oulu, Finland, Aug. 2005, pp. 17–18.
- [21] H. A. Yang and W. Fang, "On the scale effect of magnetic induction heating for microstructure," in *Proc. Transducers*, Seoul, Korea, Jul. 2005, pp. 2123–2126.
- [22] H. Benson, *University Physics*. New York: Wiley, 1996.
- [23] A. G. Guy, *Introduction to Materials Science*. New York: McGraw-Hill, 1972.
- [24] J. W. Judy, "Magnetic microactuators with polysilicon flexures," M.S. thesis, Dept. EECS, Univ. California, Berkeley, 1994.
- [25] J. W. Judy and R. S. Muller, "Magnetic microactuation of torsional polysilicon structures," *Sens. Actuators A, Phys.*, vol. 53, no. 1–3, pp. 392–397, May 1996.
- [26] R. J. Roark, *Formulas for Stress and Strain*, 4th ed. New York: McGraw-Hill, 1965.



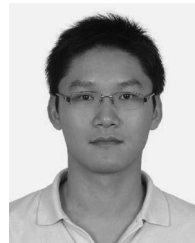
Hsueh-An Yang was born in Taipei, Taiwan, R.O.C., in 1975. He received the Ph.D. degree from National Tsing Hua University, Hsinchu, Taiwan, in 2006. His thesis was focused on the analysis and applications of electromagnetic eddy current for MEMS.

Since 2006, he has been with the Advanced Semiconductor Engineering Group, Kaohsiung, Taiwan, which is the world's biggest chip packager and assemble house, as a Research Staff Member. He is currently involved in various projects such as localized induction heating for wafer-level packaging and integrated passive devices of systems in package. His research interests include the characterization of eddy current in microscale, localized induction heating for micropackaging, microassemble technology, wafer bonding technology, and magnetic microactuators.



Tsung-Lin Tang was born in Kaohsiung, Taiwan, R.O.C., in 1983. He received the B.E. degree from National Taiwan Ocean University, Keelung, Taiwan, in 2005. He is currently working toward the M.S. degree at the Department of Power Mechanical Engineering, National Tsing Hua University, Hsinchu, Taiwan.

His research interests include the implementation of MEMS scanner and the applications of eddy current, Lorentz force, and magnetostatic force on microactuators.



Sheng-Ta Lee was born in Kaohsiung, Taiwan, R.O.C., in 1981. He received the B.E. degree from National Chung Hsing University, Taichung, Taiwan, in 2004 and the M.S. degree from National Tsing Hua University, Hsinchu, Taiwan, in 2006. His master's thesis was focused on the development of thin film residual stress using MEMS techniques.

His research interests include the characterization of material properties and the mechanics of MEMS device and structures.



Weileun Fang was born in Taipei, Taiwan, R.O.C., in 1962. He received the Ph.D. degree from Carnegie Mellon University, Pittsburgh, PA, in 1995. His doctoral research focused on the determination of the mechanical properties of thin films using micromachined structures.

In 1995, he was a Postdoctoral Researcher at Synchrotron Radiation Research Center, Taiwan. He joined the Department of Power Mechanical Engineering, National Tsing Hua University, Hsinchu, Taiwan, in 1996, where he is currently a Professor. He is also a Faculty Member at the Institute of Microelectromechanical Systems, National Tsing Hua University. From June to September 1999, he was with Prof. Y.-C. Tai at the California Institute of Technology, Pasadena, as a Visiting Associate. He has established a MEMS testing and characterization laboratory. His current research interests include MEMS with emphasis on microfabrication/packaging technologies, microoptical systems, microactuators, and the characterization of the mechanical properties of thin films.

Dr. Fang is a member of the American Society of Mechanical Engineers.